

Single-sweep volumetric optoacoustic tomography of whole mice

SANDEEP KUMAR KALVA,^{1,2}  XOSE LUIS DEAN-BEN,^{1,2} AND DANIEL RAZANSKY^{1,2,*}

¹Institute of Pharmacology and Toxicology and Institute for Biomedical Engineering, Faculty of Medicine, University of Zurich, Zurich, Switzerland

²Institute for Biomedical Engineering, Department of Information Technology and Electrical Engineering, ETH Zurich, Zurich, Switzerland

*Corresponding author: daniel.razansky@uzh.ch

Received 4 January 2021; revised 10 March 2021; accepted 15 March 2021; posted 16 March 2021 (Doc. ID 418591); published 4 May 2021

Applicability of optoacoustic imaging in biology and medicine is determined by several key performance characteristics. In particular, an inherent trade-off exists between the acquired field-of-view (FOV) and temporal resolution of the measurements, which may hinder studies looking at rapid biodynamics at the whole-body level. Here, we report on a single-sweep volumetric optoacoustic tomography (sSVOT) system that attains whole body three-dimensional mouse scans within 1.8 s with better than 200 μm spatial resolution. sSVOT employs a spherical matrix array transducer in combination with multibeam illumination, the latter playing a critical role in maximizing the effective FOV and imaging speed performance. The system further takes advantage of the spatial response of the individual ultrasound detection elements to mitigate common image artifacts related to limited-view tomographic geometry, thus enabling rapid acquisitions without compromising image quality and contrast. We compare performance metrics to the previously reported whole-body mouse imaging implementations and alternative image compounding and reconstruction strategies. It is anticipated that sSVOT will open new venues for studying large-scale biodynamics, such as accumulation and clearance of molecular agents and drugs across multiple organs, circulation of cells, and functional responses to stimuli. © 2021 Chinese Laser Press

<https://doi.org/10.1364/PRJ.418591>

1. INTRODUCTION

Small animal models are extensively used in biomedical research to study human disease progression and monitor responses to therapies [1,2]. Several clinical imaging modalities, such as computed tomography (CT) [3], magnetic resonance imaging (MRI) [4,5], positron emission tomography (PET) [6], and pulse-echo ultrasound (US) [7,8], have been downscaled for preclinical imaging applications. Other approaches based on optical contrast have further been developed for functional and molecular imaging of mice and other rodents at the whole body level [9,10]. The optical methodologies have the particular advantage of rich functional and molecular contrast while being free of ionizing radiation [11]. Optoacoustic tomography (OAT) in particular has been gaining prominence in preclinical and clinical research [12–14] because it uniquely combines the spectral sensitivity and contrast of optical imaging with high spatial resolution provided by US [15]. Additionally, OAT systems have recently been advanced to enable two-dimensional (2D) or 3D imaging of limited areas at frame rates of hundreds to thousands of hertz [16–18].

Generally, the spatio-temporal resolution of OAT inversely scales with the field of view (FOV). Several implementations of OAT systems based on different types of light delivery methods and US detection geometries have been used for small animal

imaging. Whole-body configuration examples include linear arrays translated and rotated to cover a mouse [19], curved/arc shaped transducers rotated around the longitudinal axis of the animal [20], longitudinal translation of concave arrays with cylindrically focused elements [21,22], or sparse hemispherical arrays rotated around the central axis [23,24]. For all these configurations, imaging of the entire mouse is achieved in a relatively long time—typically tens of minutes. This hampers their applicability e.g. for pharmacokinetics and pharmacodynamics studies within a relatively large region. Alternatively, real-time imaging can be achieved in a relatively small 2D or 3D region with *ad hoc* designed US arrays tailored for an optimal OAT performance [25,26]. The unique spatio-temporal resolution provided by spherical arrays with a sufficiently dense distribution of detectors further inspired the development of spiral volumetric optoacoustic tomography (SVOT) [27,28]. This approach smartly combines high temporal resolution at selected regions with a large FOV at much lower temporal resolution, thus enabling the visualization of dynamic processes expanding across multiple spatial and temporal scales.

Here, we introduce single-sweep volumetric optoacoustic tomography (sSVOT) as what we believe, to the best of our knowledge, is a new approach for high-frame-rate imaging of large volumes in mice. This was achieved by employing a

fiber bundle bifurcated into five individual output arms arranged in a light delivery scheme that concomitantly illuminates larger portions of the mouse body. A new spherical array was also specifically designed to attain an optimal trade-off between the FOV and imaging speed. It is shown that superior image quality can be achieved by using a single vertical sweep of the array together with the proper illumination arrangement. The performance of sSVOT is assessed as a function of the reconstruction method and the scanning speed while a systematic comparison to previously reported whole-body imaging implementations is further performed.

2. MATERIALS AND METHODS

A. sSVOT Experimental Setup

The schematic of the sSVOT scanner is depicted in Fig. 1(a). An optical parametric oscillator (OPO)-based laser (SpitLight, Innolas Laser GmbH, Krailling, Germany) was used as an illumination source that provides <10 ns pulses at a repetition rate of 10 Hz over a broad tunable wavelength range of 680–1250 nm with maximum pulse energies reaching up to ~ 125 mJ at the laser output. In the current study, all the experiments were conducted by tuning the laser wavelength to 800 nm. The light beam was guided through a custom-made fiber bundle (CeramOptec GmbH, Bonn, Germany) that bifurcates into five outputs with an equal number of fibers. All five outputs were placed at the same radial distance of 40 mm from the center of a custom-made spherical array. One of them was inserted into a central cavity of the array, while the other four were arranged on both sides at angles of $\pm 64^\circ$ and $\pm 76^\circ$ using a custom-designed holder [Fig. 1(a), right]. A Gaussian illumination profile with a size of 10 mm at full width at half-maximum (FWHM) was created at the tissue surface by each bundle output, resulting in a ~ 10 mm height and ~ 31 mm arc length illumination pattern on the surface of the imaging sample when using all five outputs. The measured energy of the beam at the output end of the five-arm fiber bundle was ~ 55 mJ. This amount of energy was spread on the animal surface across an area of ~ 3.1 cm², resulting in an optical fluence of ~ 17.7 mJ/cm², which was well below ANSI safety limits in all experiments [29]. The generated optoacoustic (OA) responses were collected at multiple locations around the imaged volume with the custom-made spherical array of US sensors. This consisted of 512 elements arranged on a hemispherical cap with a 40 mm radius and an angular coverage of 110° (0.61π solid angle). Each individual element of the array has an approximate area of ~ 7 mm², central detection frequency of 7 MHz, and an FWHM bandwidth of $\sim 85\%$. The OA signals were simultaneously digitized by a custom-made parallel data acquisition unit (DAQ) (Falkenstein Mikrosysteme GmbH, Taufkirchen, Germany) at 40 megasamples per second and transferred through 1 Gb/s Ethernet connection to a PC for storage and further processing. The Q-switch output of the laser was used to trigger the DAQ. Data acquisition was controlled using a computer with MATLAB (R2020b).

B. sSVOT Scanning Procedure

sSVOT scans were carried out by continuous motion of the spherical array detector together with the output(s) of the fiber

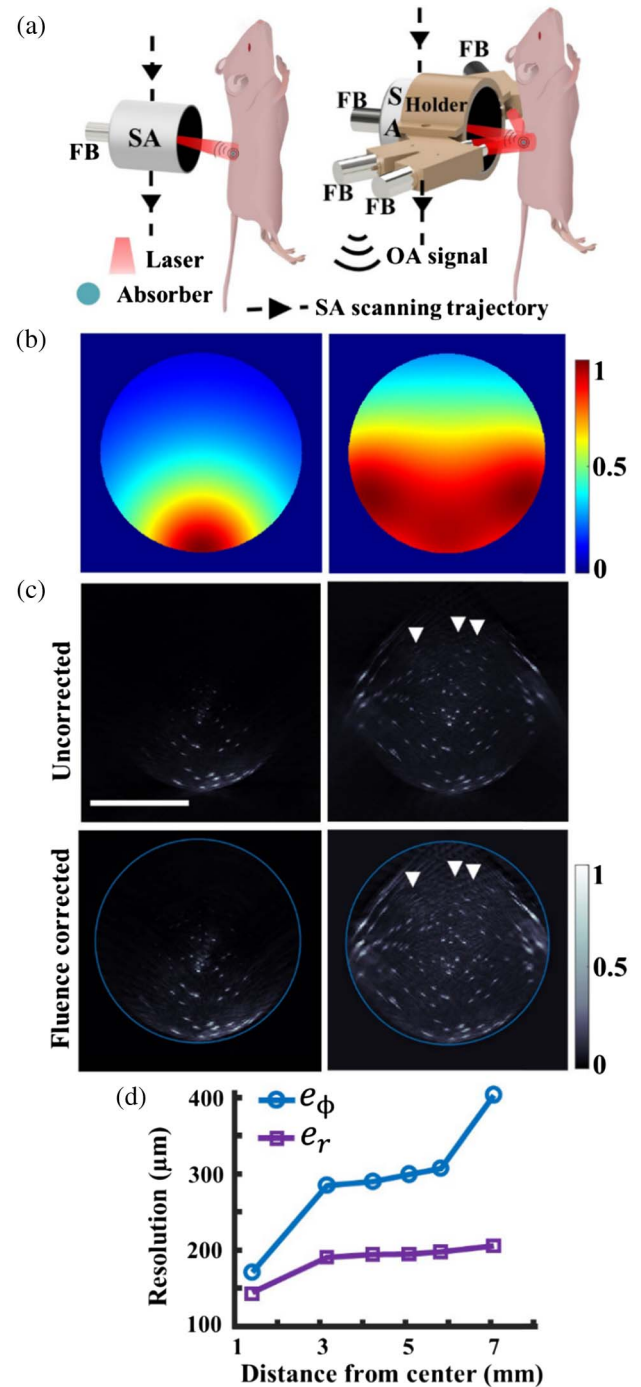


Fig. 1. Single-sweep volumetric optoacoustic tomography (sSVOT) system characterization. (a) Schematic of the sSVOT scanner showing the difference between the single-beam illumination based (left) and multi-beam illumination (right) approach. SA, spherical array; FB, fiber bundle; and OA, optoacoustic. (b) Simulated light distribution models for single-beam illumination (left) and multi-beam illumination (right). (c) Maximum intensity projections (MIPs) across cross-sectional view demonstrating the spheres using single-beam (top left) and multi-beam illumination (top right) approaches at single position of the spherical array. The corresponding fluence corrected images are shown at the bottom row. Arrows point to the spheres that appeared after the fluence correction. (d) Characterization of the reconstructed microspheres size in the central imaging plane along the radial (e_r) and azimuthal (e_ϕ) directions. Scale bar: 1 cm.

bundle along the vertical direction. In the current implementation, mice were scanned from head to tail by acquiring 10 volumes per second (dictated by the pulse repetition rate of the OPO laser). The position of the spherical array was controlled using a motorized stage that can be translated in the vertical (z) direction (RCP2-RGD6C, IAI Inc., Shizuoka Prefecture, Japan). The vertical motor has a load-bearing capacity of up to 8 kg and can cover a range of up to 15 cm with a maximum scanning velocity of 80 mm/s. There was no vibrational noise generated by the motor because the total weight of the spherical array together with fiber bundles, the associated cables, and the counter weight balance (to the transducer) was away below the maximum load capacity of the motor. The exact position of this stage was monitored with a high-resolution distance (time-of-flight position) sensor (Keyence Deutschland GmbH, Neu-Isenburg, Germany) providing a sufficiently large distance range (± 5 cm) to cover the entire mouse scan. The distance sensor was triggered in sync with the DAQ by the laser pulse trigger signal from the OPO laser and the motor positions were controlled using a computer with MATLAB (R2020b). With continuous motion of the spherical array, consecutive volumetric frames overlap for each laser pulse. Generally, higher overlapping between compounded frames is produced for slower scanning speeds, which results in an averaging effect that increases the image contrast. The pitch (distance) between neighboring frames is given by the velocity/frame rate. For example, a motor velocity of 10 mm/s and a pulse repetition rate of 10 Hz lead to a pitch of 1 mm. Considering the FOV extending over 10 mm along the vertical axis, there is $\sim 90\%$ overlap between consecutive volumes. Naturally, the signal-to-noise-ratio (SNR) depends on the number of overlapping volumes and is hence expected to be lower if the scanning velocity is increased. Higher scanning velocity diminishes the overlap between the consecutive volumetric frames, worsening the SNR and overall image quality. The dependence of the SNR on the scanning velocity is elaborated in significant detail in Ref. [30].

C. Phantom Experiments

The effectiveness of the multibeam illumination approach was initially tested using a tissue that mimicked a 20 mm cylindrical phantom consisting of agar (1.3% by weight) containing black India ink and 1.2% by volume of Intralipid to simulate a background absorption coefficient of $\mu_a = 0.23 \text{ cm}^{-1}$ and a reduced scattering coefficient of $\mu'_s = 10 \text{ cm}^{-1}$ in average biological tissues at the 800 nm excitation wavelength used in the experiments [31]. A cloud of black polyethylene absorbing microspheres (Cospheric LLC, Santa Barbara, CA, USA) approximately 100 μm in diameter was embedded into the phantom. The data was collected at a single position of the spherical array by using all five outputs of the bundle and compared against the conventional illumination configuration only employing a single direction illumination through the cavity of the array [Fig. 1(c)]. The acquired signals were averaged 100 times to achieve a better SNR.

D. Animal Experiments

In vivo animal experiments were conducted on athymic nude-Foxn1^{nu} mice in accordance with the Swiss Federal

Act on Animal Protection and with the approval of the Cantonal Veterinary Office in Zurich. The mice were placed in a fixed stationary position using a custom-made animal holder inside a water tank [27]. The water was stabilized at a 34°C temperature using a feedback-controlled heating stick throughout the experiments. During the tomographic data acquisition, the mouse remained inactive with its fore and hind paws attached to the holder and under isoflurane anesthesia (4% volume ratio for induction and 1.5% volume ratio during the experiments at Abbott, Cham, Switzerland) in an oxygen/air mixture (100/400 mL/min). The gas anesthesia was provided using a custom-made breathing mask attached to mouth clamp and the animal nose and mouth were placed above the water surface at all times. A vet ointment (Bepanthen, Bayer AG, Leverkusen, Germany) was applied on the mouse's eyes to prevent dehydration during scanning and to protect them from the laser light.

E. Image Reconstruction and Analysis

The recorded time-resolved OA signals were initially bandpass-filtered within the 0.1–12 MHz frequency range covering the entire detectable bandwidth of the transducer and deconvolved with the impulse response of the US array sensing elements [32]. Image reconstruction of individual volumetric frames was carried out using a graphics processing unit (GPU) implementation of the back-projection (BP) algorithm [33]. Note that an average speed of sound of 1486 m/s and 1525 m/s was used during the reconstruction for phantom and *in vivo* data, respectively. The voxel size was set to 30 μm and 100 μm for the phantom and mice images, respectively. Generally, each US sensing element is considered to be a single point detector for the conventional BP reconstruction algorithm. Here, we instead suggest an alternative approach where each US element is split into equally spaced subelements. The OA signal collected by a given element of the array is then assigned to the corresponding subelements, and back-projection is performed by assuming that all subelements are point sources. Note that the same signal values were assigned to all the subelements corresponding to the nearest-neighbor interpolation within a given sensing element of the array transducer. With this approach, we expect to account for the directivity of the elements; hence minimizing streak-type artifacts associated with the limited angular sensitivity and large spacing between the adjacent elements of the array [34]. Whole-mice images were obtained by compounding (stitching) the individual volumetric images for each scan position of the spherical array transducer. Several compounding techniques such as addition, maximum, and inverse center distance weighting (ICDW) were considered for this purpose [35]. Taking $v_s(x, y, z)$ as the compounded (stitched) image and $v_i(x, y, z), i = 1, 2, \dots, N$ as the individual volumes, the addition compounding method involves simply summing up the consecutive volumetric images after proper translation; i.e.,

$$v_s(x, y, z) = \sum_{i=1}^N v_i(x, y, z), \quad (1)$$

whereas the maximum compounding method considers the maximum intensities between consecutive volumes after proper translation; i.e.,

$$v_i(x, y, z) = \max_{i=1 \text{ to } N} \{v_i(x, y, z)\}. \quad (2)$$

The ICDW algorithm considers weighting the voxels in each individual volume according to the distance from the center of the respective volume, then adding the individual volumes after proper translation and normalizing them with the sum of all weights for each voxel in the compounded volume. This operation is described as

$$v_i(x, y, z) = \begin{cases} \frac{\sum_{i=1}^N w_i(x, y, z) v_i(x, y, z)}{\sum_{i=1}^N w_i(x, y, z)}, & \text{if } \forall i: d_i(x, y, z) \neq 0, \\ v_i(x, y, z), & \text{if } \exists i: d_i(x, y, z) = 0, \end{cases} \quad (3)$$

with $w_i(x, y, z) = [d_i(x, y, z)]^{-k}$,

where w_i is the weight of the voxel depending on the distance d_i from the center of the individual volume v_i .

3. RESULTS

A. Multibeam Illumination Approach

The multibeam illumination approach based on a fiber bundle with five output arms significantly enhances the homogeneity of light intensity throughout the sample. For better comprehension, we have shown the approximate simulations of the 2D light distribution over a 20 mm diameter circular region simulating a typical cross-section of the mouse, based on superimposing exponentially decaying functions of the form $e^{-\sqrt{3\mu_a(\mu_a+\mu_s)}z}$, for each output fiber bundle [Fig. 1(b)]. The simulations were executed on a grid with $\sim 33 \mu\text{m}/\text{pixel}$ resolution. The initial points of light delivery for a single-beam and

multibeam illumination were chosen on the circumference of the circle having a ~ 10 mm wide strip at the respective angular position of each fiber bundle. Clearly, more homogenous light illumination allows us to fully exploit the effective FOV of the spherical array. Only a small part of a tissue-mimicking phantom containing sparsely distributed spheres was visible at a single position of the spherical array when using single-beam illumination [Fig. 1(c), left]. However, the entire phantom could be covered with the multibeam illumination [Fig. 1(c), right], which facilitated discernment of nearly all the microspheres. After employing fluence correction using the exponentially decaying function, some of the spheres (pointed with arrows) were only discerned in the corrected images [Fig. 1(c), bottom row] in contrast to the uncorrected ones [Fig. 1(c), top row]. Note that the microspheres have a much stronger absorption coefficient than the surrounding background mimicking the average optical tissue properties. After fluence correction, we were able to fully visualize microspheres in addition to the partially visible phantom background up to ~ 20 mm depth using the multibeam illumination approach [Fig. 1(c), bottom right], whereas a limited effective penetration depth of < 10 mm was observed with the single-beam illumination approach [Fig. 1(c), bottom left]. Note that the spheres on the edge of the phantom were distorted compared to the ones in the center due to limited-view effects and directivity of the elements, which lead to degradation of the spatial resolution provided by the spherical array. The latter performance was estimated along the radial (e_r) and azimuthal (e_ϕ) directions as a function of the radial distance from the center by imaging a $30 \mu\text{m}$ sphere at different positions across the FOV. The spatial resolution of the system (size of the reconstructed microsphere)

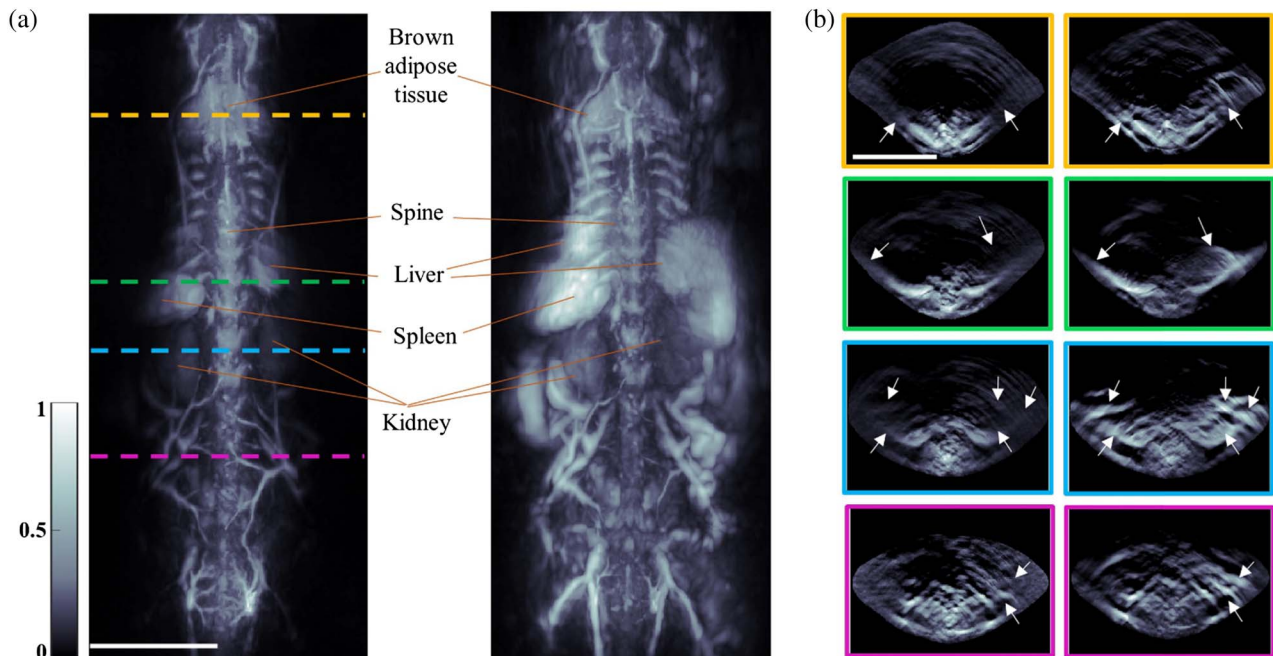


Fig. 2. *In vivo* comparison study between the single-beam and multibeam illumination approaches. (a) Images reconstructed after single vertical sweeps using single-beam (left) and multibeam (right) illuminations. (b) Fluence corrected cross-sectional reconstructions (MIPs over 1 mm thickness) at several anatomical positions along the animal: (left) using single-beam and (right) using multibeam illumination. Arrows point to the differences. Scale bar: 1 cm.

along the radial and azimuthal directions ranged from 130–200 μm to 170–400 μm , respectively [Fig. 1(d)].

B. Whole-Body Mouse Scans

The benefits of the optimized illumination approach become more obvious in the mouse scans. Particularly, *in vivo* images of mice acquired with the multibeam illumination cover a significantly larger FOV than what is achieved with single-beam illumination [Fig. 2(a)]. Multibeam illumination enabled visualizing the entire back area of the mouse including major organs such as the liver, kidneys, and spleen with one vertical sweep of the array at a 10 mm/s scan speed (6.9 s total scan time), while only the spinal cord and surrounding structures were visible in the images acquired with the same scan using single-beam illumination. The differences become more evident in the maximum intensity projections (MIPs) of several slices (1 mm thickness) at different anatomical cross-sections of the animal, as shown in Fig. 2(b). All the cross-sectional images were fluence corrected with an exponentially decaying function to compensate for light attenuation with depth. This enabled clear delineation of anatomical structures over a larger area of the animal using a multibeam illumination configuration compared to single-beam illumination. A larger portion of brown adipose tissue (row 1) and other major organs such as the spleen and liver (row 2), whole kidney (row 3), and surrounding vasculature, were clearly discernable using sSVOT. Note that the organs were identified based on their expected location and anatomical appearance [36–38]. Several blood vessels in the kidney (row 3) and sacrum (row 4) regions, which were unnoticeable when using a single-beam illumination, could be clearly seen in the images with multibeam illumination.

We further analyzed the quality of the sSVOT images obtained with vertical scans at different azimuthal positions around the animal, as shown in Fig. 3. The images displayed correspond to single vertical scans made with a 10 mm/s speed at different viewing angles such as front, left back, back, and right back. The multibeam illumination approach can also enhance the dynamic range in cross-sectional views. A comparison study was done by pure rotation of the spherical array together with single-beam and multibeam illumination around 360° [schematic shown in Fig. 4(a)] at angular steps of 40° with a total of nine azimuthal angles. Several cross-sectional images obtained using multibeam illumination reveal complete anatomical information throughout the animal body while some deeply embedded structures remain indiscernible in the single-beam illumination scans [Fig. 4(b)].

C. Reconstruction Methods

The algorithms employed for image formation also affect the performance of sSVOT. Generally, OAT image reconstruction is performed with back-projection algorithms assuming point-like US sensors. However, the finite aperture (size) of the individual elements of the sSVOT spherical array leads to a limited angular sensitivity dictated by acoustic diffraction [Fig. 5(a)]. This implies that back-projected signals at larger angles barely contribute to image formation and rather generate streak-type artifacts in the images, presumably due to sparse sampling in 3D [39–41]. To mitigate this effect, all the reconstructions of the *in vivo* data were performed by splitting each element of the spherical array into 16 equally spaced subelements and then back-projecting the signals from each of these subelements considering them as point detectors [34]. Generally, several streak

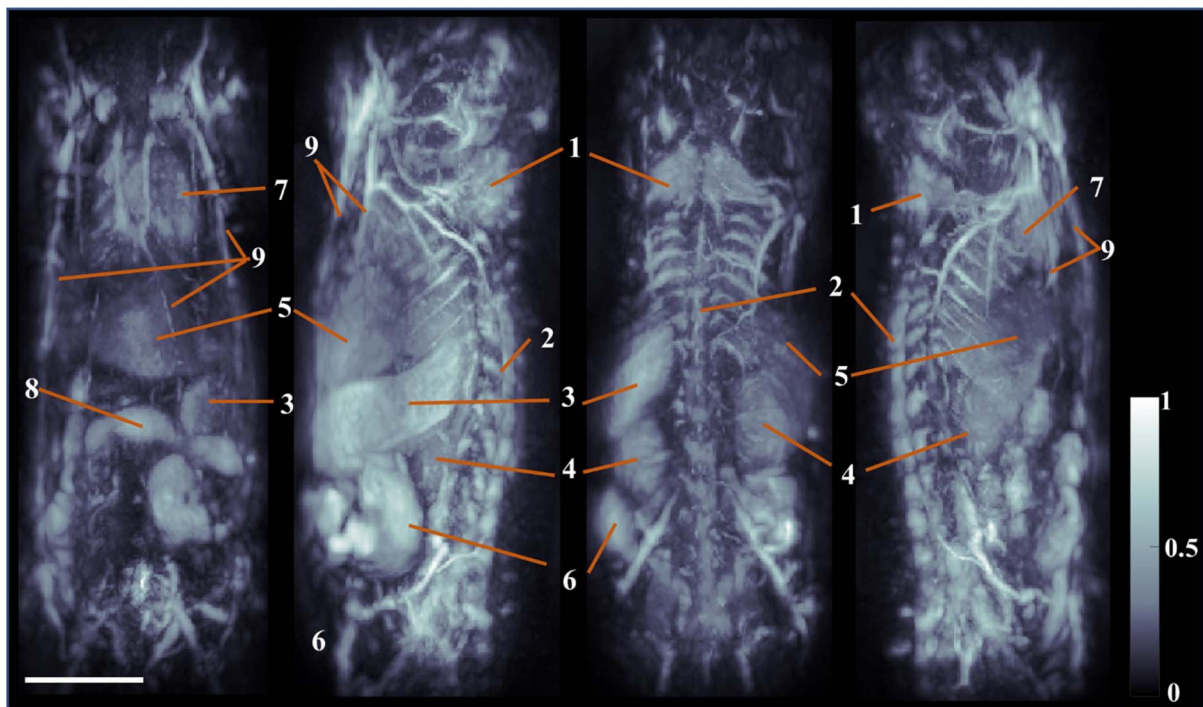


Fig. 3. sSVOT images acquired from different viewing angles (from left to right: front, left back, back, right back) at a 10 mm/s scan speed (6.9 s total scan time per compounded image) with the 16× subelements and icmax compounding method: 1, brown adipose tissue; 2, spinal cord; 3, spleen; 4, kidney; 5, liver; 6, cecum; 7, heart; 8, duodenum; and 9, thoracic vessels. Scale bar: 1 cm.

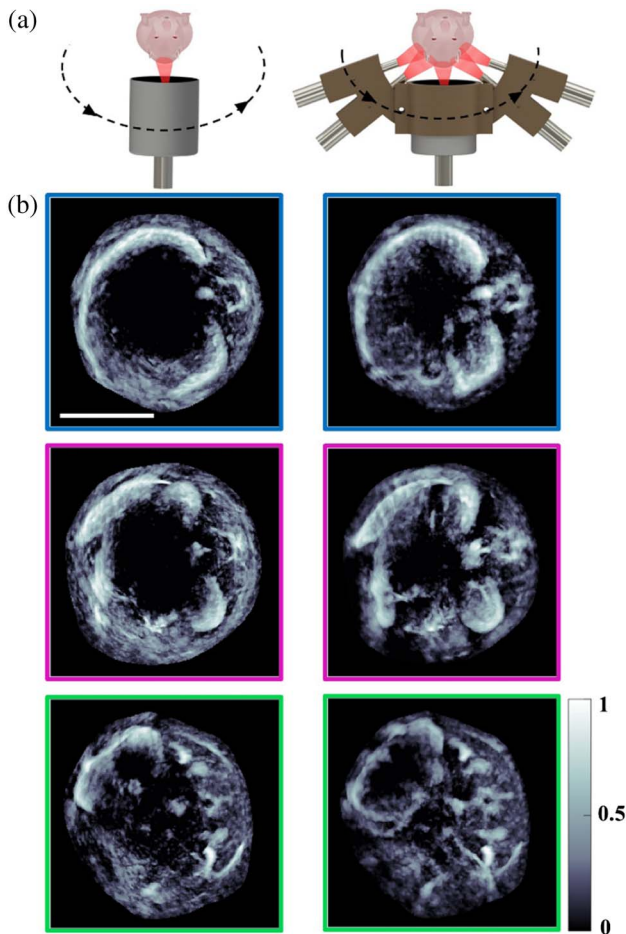


Fig. 4. Cross-sectional image quality improvement with multibeam illumination for full rotation acquisitions. (a) Schematic set up (top view) for the full (360°) rotation of the spherical array using single-beam (left) and multibeam illumination (right). (b) Corresponding cross-sectional MIP images reconstructed over a 3 mm thickness at various elevational anatomical positions. Scale bar: 1 cm.

artifacts appear when each sensing element of the array is considered as a single point detector [1×, Fig. 5(b)]. This degrades the contrast of the reconstructed volume at a single position of the spherical array [corresponding MIPs in Fig. 3(b)]. By splitting each sensing element of the array into 4, 9, and 16 subelements [Fig. 5(b)], the streak artifacts were reduced, thus revealing the underlying organs and their surrounding vasculature [Figs. 5(c)]. The contrast-to-noise ratio (CNR) in the reconstructed images was calculated via [42]

$$\text{CNR} = \frac{\mu_{\text{roi}} - \mu_{\text{back}}}{\sqrt{\frac{\sigma_{\text{roi}}^2 + \sigma_{\text{back}}^2}{2}}}, \quad (4)$$

where μ and σ are the mean and standard deviation and “roi” and “back” represent the region of interest and background, respectively. The CNR values were 4.17, 6.73, 7.3, and 7.9 for 1×, 4×, 9×, and 16× reconstructed images. Thereby, a CNR improvement of 1.6 fold using 4×, 1.8 fold using 9×, and 1.9 fold using 16× subelements was achieved compared to reconstructions done without element subdivision [Fig. 5(d)].

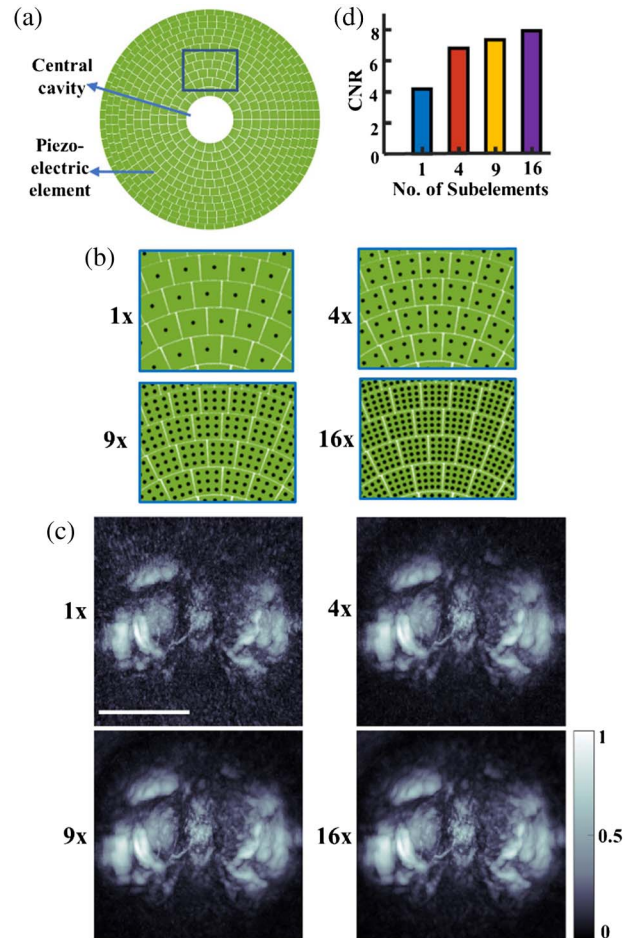


Fig. 5. Different reconstruction methods using subelement based back-projection algorithm. (a) Illustration of the spherical array with 512 sensing elements. (b) Subelement divisions used by the reconstruction algorithm are shown in zoom-ins: 1×, 4×, 9×, and 16× for each detecting element of the array. (c) Reconstructed image volumes (MIPs) across coronal view for a single position of the spherical array using element division into 1, 4, 9, and 16 subelements. (d) CNR comparison plot for various subelement-based reconstruction methods. Scale bar: 1 cm.

The quality of the whole-body mouse images corresponding to a single-sweep vertical scan is also afflicted by the method employed to compound individual reconstructed volumes at each scan position of the array. Here, we compared the performance of sSVOT for various compounding techniques like summation (sum), inverse center distance weighting (ICDW), maximum (max), sum with weighted max (sumax), and ICDW with weighted max (icmax), as shown in Fig. 6. Using sum and ICDW methods, large structures were retained in the final compounded volume; e.g., the kidney [white arrows in region-of-interest 1 (ROI1)] and sacrum (white arrows in ROI2). However, smaller blood vessels (blue arrows in ROI1, ROI2, and ROI3) could not be discerned. The max compounding method retained these smaller blood vessels at the expense of a lack of visibility of the large structures/organ such as the kidneys. The spinal cord (green arrows in ROI1 and ROI2) and the sacrum (white arrow in ROI2) were also dis-

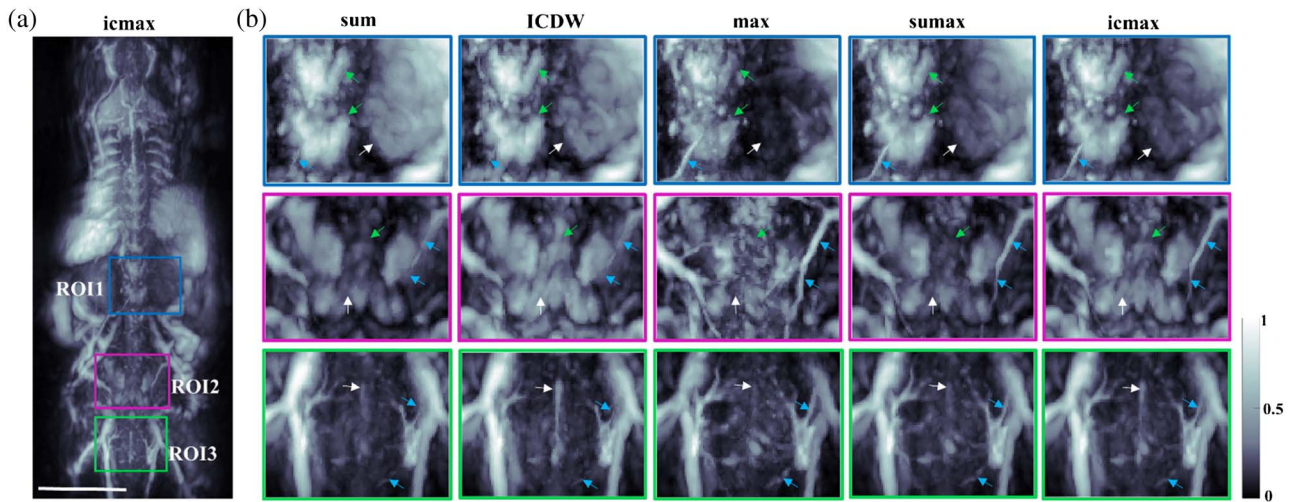


Fig. 6. Performance comparison of sSVOT reconstruction performed with different compounding methods: summation (sum), inverse center distance weighting (ICDW), maximum (max), sum with weighted max (sumax), and ICDW with weighted max (icmax). (a) sSVOT reconstructed image using icmax compounding method. Scale bar: 1 cm. (b) Zoomed-in regions of interest (ROI1, ROI2, and ROI3) compare the differences when employing various volume compounding techniques. Arrows point to the differences.

torted in shape. To preserve both large and small structural information in the final compounded volume, we combined the sum and ICDW with the weighted max (sumax and icmax, respectively). For the sumax method, the final compounded volume (FCV) of max method was weighted with the ratio of maximum intensities of FCV of the sum method to that of the max method. This weighted max volume was then added to the FCV of sum method. Similarly, for the icmax method, the FCV of the max method was weighted with the ratio of the maximum intensities of the FCV of the ICDW method to that of the max method. This weighted max volume was then added to the FCV of the ICDW method. This enabled us to retain all

the smaller blood vessels in the final compounded volume together with the large structures, as evident in the selected ROIs. Note, however, that the ICDW method generally rendered more uniform contrast compared to the sum method. The sacrum was fully visible with better contrast with ICDW (white arrow in ROI2). Also, a blood vessel (white arrow in ROI3) invisible in the image rendered with the sum method is clearly visible using ICDW. Similar enhancement was achieved with icmax compared to sumax. The icmax compounding method then appears to outperform other compounding methods in terms of preserving both large and small structural information with more uniform contrast.

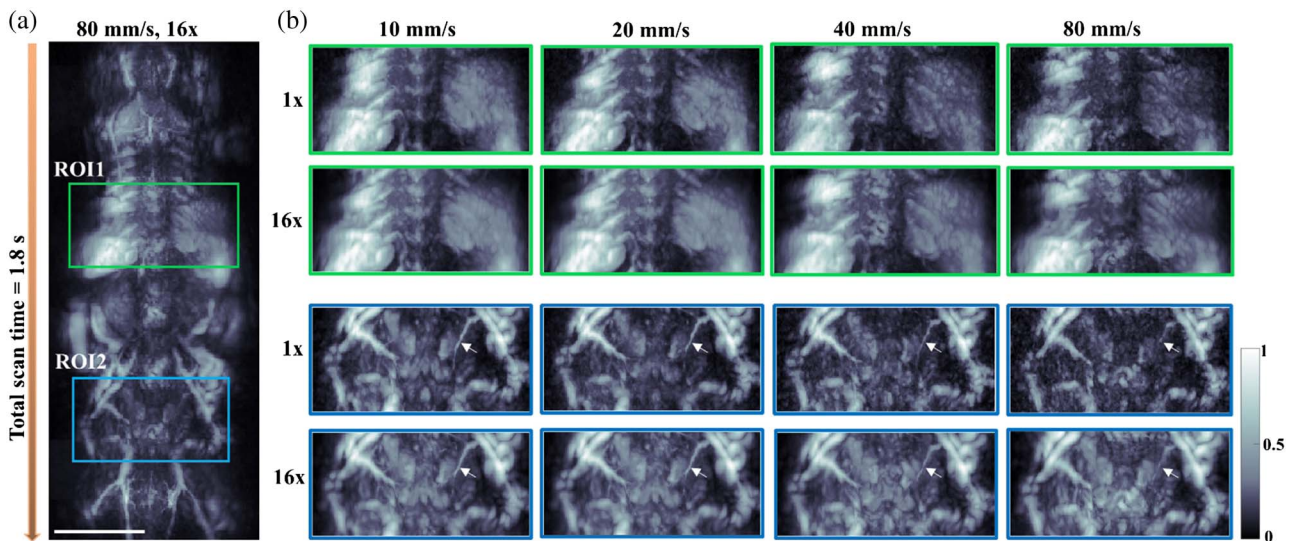


Fig. 7. Performance comparison of sSVOT system for different scan velocities of 10, 20, 40, and 80 mm/s and subelement-based reconstructions. (a) Reconstructed mice volume for a single vertical sweep at a 80 mm/s scan speed using 16x subelement division with the icmax compounding method. Scale bar: 1 cm. (b) Zoomed-in regions of interest (ROI1 and ROI2) compare different scan velocities with the 1x and 16x subelement reconstruction methods.

D. Rapid Single-Sweep Scans

High temporal resolution is essential for many studies involving rapid biodynamics; e.g., contrast agent kinetics across multiple organs, tracking of cells, or hemodynamic responses to stimuli. Due to its enhanced FOV covering the entire width of the animal, sSVOT facilitates the visualization of multiple organs like the spleen, liver, kidneys, and brown adipose tissue, and their surrounding vasculature across the whole body of mice with a single vertical sweep of the array. The temporal resolution achieved with sSVOT was analyzed by characterizing its performance for different scan speeds of 10, 20, 40, and 80 mm/s (Fig. 7). Reconstruction was performed by considering point-like sensors ($1\times$) and by splitting each sensor into 16 subelements ($16\times$). The icmax compounding method was employed for all reconstructions. For scan speeds of 10 and 20 mm/s, both $1\times$ and $16\times$ subelement reconstruction methods yielded similar image contrast and all the large structures, like the spleen, liver, spinal cord (ROI1), sacrum, and the larger and smaller blood vessels (ROI2), were clearly discernable. However, at scan speeds of 40 and 80 mm/s, the contrast of the spleen, liver, and sacrum was diminished when using $1\times$ element reconstruction compared to that achieved for 10 and 20 mm/s (ROI1 and ROI2). The contrast of spinal cord (ROI1) was also reduced at 40 mm/s and became barely visible at the 80 mm/s scan speed. Moreover, the smaller blood vessels (white arrows) in ROI2 were partially visible with 40 mm/s and became completely invisible at the 80 mm/s scan speed. Nevertheless, with an increased number of subelements ($16\times$), the contrast was largely restored at the 40 and 80 mm/s scan speeds. For example, the contrast in ROI1 and ROI2 was similar to that obtained with a $1\times$ element at a 10 mm/s scan speed. Moreover, the smaller blood vessels can be clearly seen with $16\times$ subelement reconstruction at a 40 mm/s scan speed but are barely visible at 80 mm/s. It appears that the $16\times$ reconstruction method has a similar effect on the reduction of streak artifacts as the effect of reducing scanning speed corresponding to a larger degree of overlap between the single acquired volumes. Overall, sSVOT enables visualizing multiple organs and their surrounding major vasculature structures at a high scan speed of 80 mm/s with 1.8 s scan time.

4. DISCUSSION AND CONCLUSIONS

The single-vertical sweep protocol of the sSVOT imaging scanner introduced in this work offers what we believe are new venues to study rapid biodynamics. The multibeam illumination approach used in sSVOT played a critical role in expanding the FOV, achieving deeper penetration into the animal body and improving the overall image quality and speed. With these advantages, multiple organs and surrounding vascular structures could be imaged across the whole body of a mouse, from head to tail. Scan speeds of up to 80 mm/s, leading to a temporal resolution of 1.8 s, are far beyond what is achievable with other whole-body preclinical imaging modalities. We believe this high-speed imaging could be of particular importance in many applications, such as in cancer research for assessing vascular perfusion function or for studying accumulation and retention of nanodrug formulations in tumors [43]. By visualizing multiple contrast agent kinetics simultaneously throughout the

mouse body, sSVOT may play a major role in other molecular imaging and drug development applications.

Generally, a trade-off between FOV and spatial resolution is expected in any OA imaging embodiment [15,44]. The spherical array employed in the sSVOT scanner provides an almost isotropic resolution of $\sim 130\ \mu\text{m}$ at the center of the FOV, which progressively degrades at laterally shifted positions [32]. Note also that the limited-view effects are, more likely to affect the peripheral regions of the mouse [45]. Those can be mitigated by increasing the angular coverage of the spherical array; however, this is detrimental to the effectively covered FOV. The frequency and angular coverage of the newly designed array were selected to efficiently cover the entire width of the mouse. A better tomographic coverage and higher resolution within the entire mouse body can be achieved by laterally scanning and/or rotating the array around the animal. We have shown that high-quality, cross-sectional images could be obtained by rotating the array for 360° at a total of nine azimuthal angles, which can still be performed in a relatively short time.

Optimal selection of the image formation method was also vital to improve the quality of the images. A comparison of the performance of the sSVOT for different reconstruction methods and scan speeds showed that the ICDW compounding with the weighted maximum method outperformed other compounding methods and that the $16\times$ subelement back-projection reconstruction method could mitigate the streak artifacts that appeared with the $1\times$ -element back-projection reconstruction in fast scans. More advanced reconstruction approaches (e.g., based on spatiotemporal antialiasing method) [40,41] or model-based (iterative) methods, can further help improve image quality at the expense of longer computation times [39,46]. However, the back-projection reconstruction has the clear advantage of real-time image rendering, even when multiple subelements are considered. This enables an on-the-fly preview during acquisitions, which is important to optimize the experimental measurements.

Another key aspect to be taken into account is the object's motion (e.g., related to heartbeat or respiration). For a high scan speed of 80 mm/s and a 10 Hz pulse repetition rate (PRF) of the laser, the array moves $\sim 8\ \text{mm}$ between consecutive laser pulses, while each reconstructed frame covers $\sim 10\ \text{mm}$ in the vertical direction. Therefore, only a 20% volume overlap exists between the consecutive frames. Motion artifacts are then generally manifested as structural inaccuracies in the compounded images rather than as blurring and loss of resolution and contrast, as is the case when scanning the array at lower speeds or using a higher PRF. Respiratory motion suppression algorithms [47] and/or gated acquisition approaches [48–50] may further be employed to enhance image quality by mitigating the common motion artifacts in the compounded images.

In summary, sSVOT achieves rapid scanning of a large portion of the mouse body with excellent image contrast and resolution. The multibeam illumination approach was shown to be essential to enhance the achievable FOV and effective penetration. We exploited the system for large-scale imaging of mice with a single vertical sweep of a spherical array, demonstrating the feasibility of visualizing multiple organs and their

surrounding vasculature without the need for signal averaging. We believe that sSVOT has the potential to massively impact biomedical studies focusing on whole-body imaging of rapid biological dynamics.

Funding. European Research Council (ERC-2015-CoG-682379).

Acknowledgment. The authors would like to thank M. Reiss for his support with the measurements and animal handling, and H. Estrada, U. A. T. Hofmann, A. Ozbek, B. Lafci, and S. Nitkunanantharajah for their valuable advice.

Disclosures. The authors declare no conflicts of interest.

Data availability. Data underlying the results presented in this paper are not publicly available at this time but may be obtained from the authors upon reasonable request.

REFERENCES

1. F. Kiessling and B. J. Pichler, *Small Animal Imaging: Basics and Practical Guide* (Springer, 2010).
2. M. Baker, "The whole picture," *Nature* **463**, 977–979 (2010).
3. C. Badea, M. Drangova, D. W. Holdsworth, and G. A. Johnson, "In vivo small-animal imaging using micro-CT and digital subtraction angiography," *Phys. Med. Biol.* **53**, R319–R350 (2008).
4. R. G. Pautler and S. C. Fraser, "The year(s) of the contrast agent—micro-MRI in the new millennium," *Curr. Opin. Immunol.* **15**, 385–392 (2003).
5. H. Benveniste and S. Blackband, "MR microscopy and high resolution small animal MRI: applications in neuroscience research," *Prog. Neurobiol.* **67**, 393–420 (2002).
6. H. R. Herschman, "Micro-PET imaging and small animal models of disease," *Curr. Opin. Immunol.* **15**, 378–384 (2003).
7. L. A. Wirtzfeld, G. Wu, M. Bygrave, Y. Yamasaki, H. Sakai, M. Moussa, J. I. Izawa, D. B. Downey, N. M. Greenberg, A. Fenster, J. W. Xuan, and J. C. Lacefield, "A new three-dimensional ultrasound microimaging technology for preclinical studies using a transgenic prostate cancer mouse model," *Cancer Res.* **65**, 6337–6345 (2005).
8. A. Greco, M. Mancini, S. Gargiulo, M. Gramanzini, P. P. Claudio, A. Brunetti, and M. Salvatore, "Ultrasound biomicroscopy in small animal research: applications in molecular and preclinical imaging," *J. Biomed. Biotechnol.* **2012**, 519238 (2012).
9. A. H. Hielscher, "Optical tomographic imaging of small animals," *Curr. Opin. Biotechnol.* **16**, 79–88 (2005).
10. M. Yang, E. Baranov, P. Jiang, F.-X. Sun, X.-M. Li, L. Li, S. Hasegawa, M. Bouvet, M. Al-Tuwaijri, T. Chishima, H. Shimada, A. R. Moossa, S. Penman, and R. M. Hoffman, "Whole-body optical imaging of green fluorescent protein-expressing tumors and metastases," *Proc. Natl. Acad. Sci. USA* **97**, 1206–1211 (2000).
11. F. Leblond, S. C. Davis, P. A. Valdés, and B. W. Pogue, "Pre-clinical whole-body fluorescence imaging: review of instruments, methods and applications," *J. Photochem. Photobiol. B* **98**, 77–94 (2010).
12. P. Beard, "Biomedical photoacoustic imaging," *Interface Focus* **1**, 602–631 (2011).
13. S. Manohar and D. Razansky, "Photoacoustics: a historical review," *Adv. Opt. Photon.* **8**, 586–617 (2016).
14. M. Heijblom, D. Piras, M. Brinkhuis, J. C. G. van Hespén, F. M. van den Engh, M. van der Schaaf, J. M. Klaase, T. G. van Leeuwen, W. Steenbergen, and S. Manohar, "Photoacoustic image patterns of breast carcinoma and comparisons with magnetic resonance imaging and vascular stained histopathology," *Sci. Rep.* **5**, 11778 (2015).
15. L. V. Wang and S. Hu, "Photoacoustic tomography: in vivo imaging from organelles to organs," *Science* **335**, 1458–1462 (2012).
16. X. L. Dean-Ben, S. J. Ford, and D. Razansky, "High-frame rate four dimensional optoacoustic tomography enables visualization of cardiovascular dynamics and mouse heart perfusion," *Sci. Rep.* **5**, 10133 (2015).
17. A. Özbek, X. L. Deán-Ben, and D. Razansky, "Optoacoustic imaging at kilohertz volumetric frame rates," *Optica* **5**, 857–863 (2018).
18. K. Sivasubramanian and M. Pramanik, "High frame rate photoacoustic imaging at 7000 frames per second using clinical ultrasound system," *Biomed. Opt. Express* **7**, 312–323 (2016).
19. J. Gateau, M. A. A. Caballero, A. Dima, and V. Ntziachristos, "Three-dimensional optoacoustic tomography using a conventional ultrasound linear detector array: whole-body tomographic system for small animals," *Med. Phys.* **40**, 013302 (2013).
20. H.-P. F. Brecht, R. Su, M. Fronheiser, S. A. Ermilov, A. Conjusteau, and A. A. Oraevsky, "Whole-body three-dimensional optoacoustic tomography system for small animals," *J. Biomed. Opt.* **14**, 064007 (2009).
21. J. Xia, M. R. Chatni, K. Maslov, Z. Guo, K. Wang, M. Anastasio, and L. V. Wang, "Whole-body ring-shaped confocal photoacoustic computed tomography of small animals in vivo," *J. Biomed. Opt.* **17**, 050506 (2012).
22. D. Razansky, A. Buehler, and V. Ntziachristos, "Volumetric real-time multispectral optoacoustic tomography of biomarkers," *Nat. Protoc.* **6**, 1121–1129 (2011).
23. R. Kruger, D. Reinecke, G. Kruger, M. Thornton, P. Picot, T. Morgan, K. Stantz, and C. Mistretta, "HYPR-spectral photoacoustic CT for pre-clinical imaging," *Proc. SPIE* **7177**, 71770F (2009).
24. J. Lv, Y. Peng, S. Li, Z. Guo, Q. Zhao, X. Zhang, and L. Nie, "Hemispherical photoacoustic imaging of myocardial infarction: in vivo detection and monitoring," *Eur. Radiol.* **28**, 2176–2183 (2018).
25. X. L. Deán-Ben and D. Razansky, "Adding fifth dimension to optoacoustic imaging: volumetric time-resolved spectrally enriched tomography," *Light Sci. Appl.* **3**, e137 (2014).
26. S. Gottschalk, T. F. Fehm, X. L. Deán-Ben, and D. Razansky, "Noninvasive real-time visualization of multiple cerebral hemodynamic parameters in whole mouse brains using five-dimensional optoacoustic tomography," *J. Cereb. Blood Flow Metab.* **35**, 531–535 (2015).
27. T. F. Fehm, X. L. Deán-Ben, S. J. Ford, and D. Razansky, "In vivo whole-body optoacoustic scanner with real-time volumetric imaging capacity," *Optica* **3**, 1153–1159 (2016).
28. X. L. Deán-Ben, T. F. Fehm, S. J. Ford, S. Gottschalk, and D. Razansky, "Spiral volumetric optoacoustic tomography visualizes multi-scale dynamics in mice," *Light Sci. Appl.* **6**, e16247 (2017).
29. "American National Standard for safe use of lasers," ANSI Z136.1-2007 (American National Standards Institute, 2007).
30. A. Ron, S. K. Kalva, V. Periyasamy, X. L. Deán-Ben, and D. Razansky, "Flash scanning volumetric optoacoustic tomography for high resolution whole-body tracking of nanoagent kinetics and biodistribution," *Laser Photon. Rev.* **15**, 2000484 (2021).
31. S. L. Jacques, "Optical properties of biological tissues: a review," *Phys. Med. Biol.* **58**, R37–R61 (2013).
32. X. L. Dean-Ben and D. Razansky, "Portable spherical array probe for volumetric real-time optoacoustic imaging at centimeter-scale depths," *Opt. Express* **21**, 28062–28071 (2013).
33. X. L. Dean-Ben, A. Ozbek, and D. Razansky, "Volumetric real-time tracking of peripheral human vasculature with GPU-accelerated three-dimensional optoacoustic tomography," *IEEE Trans. Med. Imaging* **32**, 2050–2055 (2013).
34. S. K. Kalva and M. Pramanik, "Experimental validation of tangential resolution improvement in photoacoustic tomography using a modified delay-and-sum reconstruction algorithm," *J. Biomed. Opt.* **21**, 086011 (2016).
35. S. Nitkunanantharajah, C. Hennesperger, X. L. Dean-Ben, D. Razansky, and N. Navab, "Trackerless panoramic optoacoustic imaging: a first feasibility evaluation," *Int. J. Comput. Assist. Radiol. Surg.* **13**, 703–711 (2018).
36. S. Cinti, "The adipose organ at a glance," *Dis. Models Mech.* **5**, 588–594 (2012).
37. A. Karlas, J. Reber, E. Liapis, K. Paul-Yuan, and V. Ntziachristos, "Multispectral optoacoustic tomography of brown adipose tissue," in *Brown Adipose Tissue* (Springer, 2018), pp. 325–336.

38. A. Ron, X. L. Deán-Ben, J. Reber, V. Ntziachristos, and D. Razansky, "Characterization of brown adipose tissue in a diabetic mouse model with spiral volumetric optoacoustic tomography," *Mol. Imaging Biol.* **21**, 620–625 (2019).
39. X. L. Deán-Ben, A. Buehler, V. Ntziachristos, and D. Razansky, "Accurate model-based reconstruction algorithm for three-dimensional optoacoustic tomography," *IEEE Trans. Med. Imaging* **31**, 1922–1928 (2012).
40. P. Hu, L. Li, L. Lin, and L. V. Wang, "Spatiotemporal antialiasing in photoacoustic computed tomography," *IEEE Trans. Med. Imaging* **39**, 3535–3547 (2020).
41. L. Li, L. Zhu, C. Ma, L. Lin, J. Yao, L. Wang, K. Maslov, R. Zhang, W. Chen, J. Shi, and L. V. Wang, "Single-impulse panoramic photoacoustic computed tomography of small-animal whole-body dynamics at high spatiotemporal resolution," *Nat. Biomed. Eng.* **1**, 0071 (2017).
42. X. Song, B. W. Pogue, S. Jiang, M. M. Doyley, H. Dehghani, T. D. Tosteson, and K. D. Paulsen, "Automated region detection based on the contrast-to-noise ratio in near-infrared tomography," *Appl. Opt.* **43**, 1053–1062 (2004).
43. W. Song, Z. Tang, D. Zhang, N. Burton, W. Driessenb, and X. Chen, "Comprehensive studies of pharmacokinetics and biodistribution of indocyanine green and liposomal indocyanine green by multispectral optoacoustic tomography," *RSC Adv.* **5**, 3807–3813 (2015).
44. X. L. Deán-Ben, S. Gottschalk, B. Mc Larney, S. Shohamc, and D. Razansky, "Advanced optoacoustic methods for multiscale imaging of *in vivo* dynamics," *Chem. Soc. Rev.* **46**, 2158–2198 (2017).
45. Y. Xu, L. V. Wang, G. Ambartsoumian, and P. Kuchment, "Reconstructions in limited-view thermoacoustic tomography," *Med. Phys.* **31**, 724–733 (2004).
46. L. Ding, X. L. Deán-Ben, and D. Razansky, "Efficient 3-D model-based reconstruction scheme for arbitrary optoacoustic acquisition geometries," *IEEE Trans. Med. Imaging* **36**, 1858–1867 (2017).
47. A. Ron, N. Davoudi, X. L. Deán-Ben, and D. Razansky, "Self-gated respiratory motion rejection for optoacoustic tomography," *Appl. Sci.* **9**, 2737 (2019).
48. N. L. Ford, H. N. Nikolov, C. J. D. Norley, M. M. Thornton, P. J. Foster, M. Drangova, and D. W. Holdsworth, "Prospective respiratory-gated micro-CT of free breathing rodents," *Med. Phys.* **32**, 2888–2898 (2005).
49. S. J. Schambach, S. Bag, L. Schilling, C. Groden, and M. A. Brockmann, "Application of micro-CT in small animal imaging," *Methods* **50**, 2–13 (2010).
50. J. Xia, W. Chen, K. Maslov, M. A. Anastasio, and L. V. Wang, "Retrospective respiration-gated whole-body photoacoustic computed tomography of mice," *J. Biomed. Opt.* **19**, 016003 (2014).